

Structural analysis of a plant fatty acid amide hydrolase provides insights into the evolutionary diversity of bioactive acylethanolamides

Received for publication, November 12, 2018, and in revised form, March 20, 2019 Published, Papers in Press, March 20, 2019, DOI 10.1074/jbc.RA118.006672

Mina Aziz[‡], Xiaoqiang Wang^{‡1}, Ashutosh Tripathi^{§2}, Vytas A. Bankaitis[§], and [®] Kent D. Chapman^{‡3}

From the ‡ BioDiscovery Institute and Department of Biological Sciences, University of North Texas, Denton, Texas 76203 and [§]Department of Molecular and Cellular Medicine, Texas A&M Health Science Center, College Station, Texas 77843

Edited by Joseph M. Jez

N-Acylethanolamines (NAEs) are fatty acid derivatives that in animal systems include the well-known bioactive metabolites of the endocannabinoid signaling pathway. Plants use NAE signaling as well, and these bioactive molecules often have oxygenated acyl moieties. Here, we report the three-dimensional crystal structures of the signal-terminating enzyme fatty acid amide hydrolase (FAAH) from Arabidopsis in its apo and ligand-bound forms at 2.1- and 3.2-Å resolutions, respectively. This plant FAAH structure revealed features distinct from those of the only other available FAAH structure (rat). The structures disclosed that although catalytic residues are conserved with the mammalian enzyme, AtFAAH has a more open substrate-binding pocket that is partially lined with polar residues. Fundamental differences in the organization of the membrane-binding "cap" and the membrane access channel also were evident. In accordance with the observed structural features of the substrate-binding pocket, kinetic analysis showed that AtFAAH efficiently uses both unsubstituted and oxygenated acylethanolamides as substrates. Moreover, comparison of the apo and ligand-bound AtFAAH structures identified three discrete sets of conformational changes that accompany ligand binding, suggesting a unique "squeeze and lock" substrate-binding mechanism. Using molecular dynamics simulations, we evaluated these conformational changes further and noted a partial unfolding of a random-coil helix within the region 531-537 in the apo structure but not in the ligand-bound form, indicating that this region likely confers plasticity to the substrate-binding pocket. We conclude that the structural divergence in bioactive acylethanolamides in plants is reflected in part in the structural and functional properties of plant FAAHs.

This work was supported initially by United States Department of Energy, Office of Science, Basic Energy Sciences, Physical Biochemistry Program Grant DE-FG02-14ER15647 and continued with funding from National Science Foundation, Division of Integrative and Organismal Sciences Grant IOS-1656263 (to K. D. C.). The authors declare that they have no conflicts of interest with the contents of this article. The content is solely the responsibility of the authors and does not necessarily represent the official views of the National Institutes of Health.

This article contains Figs. S1–S5, Table S1, and Movies S1–S6.

The atomic coordinates and structure factors (codes 6DHV and 6DII) have been deposited in the Protein Data Bank (http://wwpdb.org/).

NAE⁴ signaling is a conserved lipid signaling pathway that has been functionally diversified in multicellular organisms to regulate specific developmental, physiological, and behavioral processes. These include wide-ranging processes such as lifespan in Caenorhabditis elegans (1), seedling development in Arabidopsis (2, 3), neurotransmission in mammals (4), and satiety in vertebrates (5). In all organisms examined to date, hydrolysis of the ethanolamine moiety by fatty acid amide hydrolase (FAAH) terminates the signaling functions of the NAE (6). However, important differences in fatty acid composition among organisms indicate that there are differences in the types of NAEs employed for signaling, and this may be reflected in as yet undetermined differences in the signal-terminating enzyme FAAH. For example, higher plants generally do not contain arachidonic acid, and so anandamide (the ethanolamide conjugate of arachidonic acid) is not a common NAE signaling molecule in plants (7). Instead, plants utilize NAEs with shorter acyl chains (8), and it is the oxylipin metabolites of polyunsaturated NAEs that represent the actual bioactive molecules that modulate seedling development (2, 3). Hence, endocannabinoid signaling in animals depends primarily on the regulation of the levels of C₂₀, unsubstituted NAEs by FAAH, whereas NAE signaling in plants is primarily driven by shorterchain, often oxygenated NAEs.

In plants, NAEs are most abundant in desiccated seeds, and their levels decline dramatically during seed germination and seedling establishment (9). The decline in NAE levels is primarily dependent upon hydrolysis by FAAH where FAAH activity in Arabidopsis was shown to increase during seedling establishment, consistent with the timing of NAE depletion (10). In addition to hydrolysis by FAAH, polyunsaturated NAEs (e.g. NAE 18:2 and NAE 18:3) in plants are oxygenated by various lipoxygenases (LOXs) to generate a series of NAE oxylipin derivatives with oxygenation substitutions at either position 9 or 13 of the acyl chain (11). It had been assumed that like in

¹ To whom correspondence may be addressed. Tel.: 940-565-2969; E-mail: xiaoqiang.wang@unt.edu.

² Supported by National Institutes of Health Grant GM44530 and Robert A. Welch Foundation Grant BE-0017 (to V. A. B.).

³ To whom correspondence may be addressed. Tel.: 940-565-2969; E-mail: chapman@unt.edu.

⁴The abbreviations used are: NAE, N-acylethanolamine; FAAH, fatty acid amide hydrolase; MLnFP, methyl α -linolenyl fluorophosphonate; DDM, n-dodecyl β-D-maltoside; AS, amidase signature; ABC, acyl-binding channel; MAC, membrane access channel; MD, molecular dynamics; SASA, solvent-accessible surface areas; NAE-9-HOD, 9-hydroxy-10,12-octadecadienoylethanolamide; AHL, N-acyl L-homoserine lactone; MAFP, methyl arachidonyl fluorophosphonate; LOX, lipoxygenase; BTP, Bistris propane (1,3-bis[tris(hydroxymethyl)methylamino]propane); BCA, bicinchoninic acid; OPLS, optimized potentials for liquid simulations; At, Arabidopsis thaliana.

mammals, the parent, unsubstituted NAE molecules were the biologically active components in plants; however, recent evidence suggested that it was actually the oxylipin derivatives of NAE 18:2 and NAE 18:3 that negatively impacted seedling growth (2, 3, 9). This represents a major difference in acylethanolamide signaling between plants and animals and raises the question of whether FAAH in plants has structurally diverged to accommodate the hydrolysis of both unsubstituted and oxygenated NAEs to regulate NAE signaling in plant systems.

The three-dimensional structure of rat FAAH has been instrumental in understanding the catalytic features of this enzyme and in developing small molecule therapeutic inhibitors for manipulation of the endocannabinoid system in humans (12-14). However, the evolutionary distribution of diverse acylethanolamide signaling molecules outside of vertebrates and the lack of any structural information for FAAH enzymes beyond that of rat FAAH (or humanized variants) leave an important gap in knowledge about a fundamental lipid signaling pathway in eukaryotes. Herein, we address this gap by reporting the three-dimensional structure for full-length, recombinant Arabidopsis (At)FAAH in both a ligand-free form and complexed with an irreversible inhibitor, methyl α -linolenyl fluorophosphonate (MLnFP), allowing for a mechanistic understanding of the interaction of plant FAAH with its acylethanolamide substrates.

Results and discussion

The 3D structure of AtFAAH

Full-length AtFAAH was expressed in *Escherichia coli*, purified, and crystallized in the presence of the detergent n-dodecyl β -D-maltoside (DDM). Both the apo- and MLnFP-bound AtFAAHs were crystallized in space group $P2_1$ with two and 12 molecules per asymmetric unit, respectively. The crystal structure of apo-AtFAAH was solved at 2.1-Å by molecular replacement using the transamidosome structure (Protein Data Bank (PDB) code 3KFU) (15) as a search model. The structure of AtFAAH complexed with MLnFP was determined at 3.2 Å using the apoenzyme structure as template.

AtFAAH is a homodimer with a buried surface of 1636 Å² per monomer. Each monomer consists of a twisted β -sheet surrounded by 23 α -helices (Figs. 1 and S1). Its core structure resembles that of other amidase signature (AS) enzymes with high similarity to glutamine amidotransferase subunit A (PDB code 3KFU or 2DF4) (15, 16), allophanate hydrolase (PDB code 4ISS) (17), and aryl acylamidase (PDB code 4YJ6 (18)) (Z-scores = 44.6-41.6; a higher Z-score indicates greater structural similarity) but lower similarity to rat FAAH (Z-score = 37.6) according to a comparative analysis with the Dali search server (19). The relative similarity between AtFAAH and these other amidases is shown visually as structure overlays (Fig. 2). AtFAAH contains an additional N-terminal region (1-72) with three helices and a long loop that distinguishes it from other AS family enzymes and from rat FAAH (Fig. S2).

AtFAAH is a membrane-associated protein, and its N terminus likely plays a key role in membrane binding. A, \sim 50-Å (\sim 25 Å per monomer)-long hydrophobic rim/port formed by 12

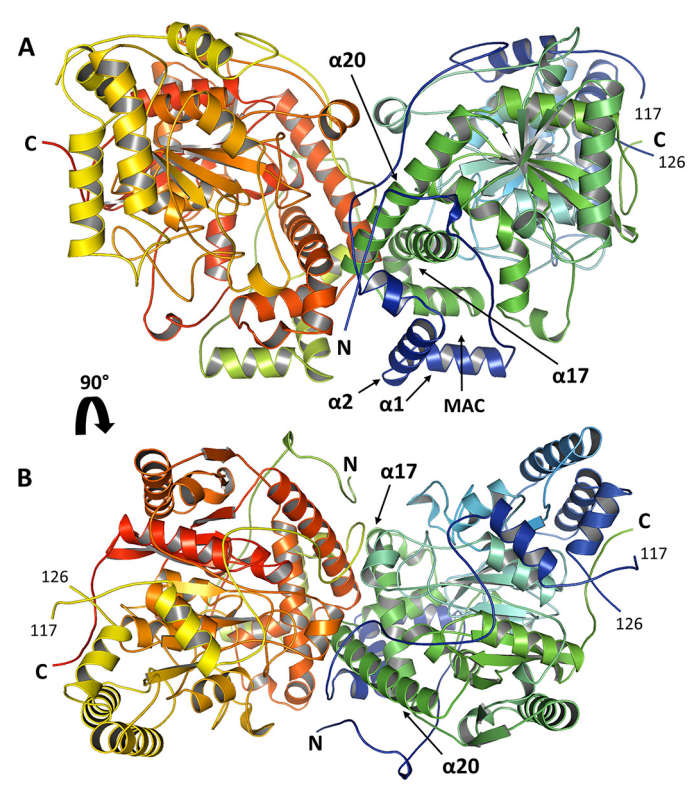


Figure 1. Arabidopsis FAAH three-dimensional structure. A and B, side (A) and top (B) views of the AtFAAH structure. AtFAAH is a homodimer assembled from 66-kDa subunits. Each subunit is shown in a color gradient ranging from blue (N terminus) to green (C terminus) for one subunit (chain A) and from yellowish-green to red for the other subunit (chain B). The presumed membrane-binding cap (α 1 and α 2) and the putative substrate entryway (MAC) are located at the N terminus of the enzyme. The AtFAAH dimer interface is formed mainly by parts of helices α 17 and α 20 and some regions of the N terminus (see Fig. 7).

hydrophobic residues, including Leu³³, Leu³⁷, Leu⁴¹, Leu⁴⁶, Ile⁴⁷, and Leu⁵⁰, which are arranged like teeth on a comb on α -helices α 1 and α 2 from both subunits, most likely forms the hydrophobic membrane-binding "cap" of AtFAAH (Fig. 3). This region is predicted to directly interact with the membrane and anchor the enzyme into the cytoplasmic leaflet of the lipid bilayer. Both sides of this hydrophobic rim/port are bounded by both hydrophobic (*e.g.* Leu³⁰, Ala⁴⁴, Pro⁴⁵, and Ile⁵¹) and hydrophilic residues (*e.g.* Ser³⁴, Lys³⁶, Asn⁴⁰, Asp⁵²³, and Lys⁵²⁶). The latter set likely interacts with phospholipid headgroups in the membrane. By contrast, rat FAAH lacks such a long N-terminal region, and its membrane-binding cap is formed by hydrophobic helices α 18 and α 19, more toward the C terminus of the protein (Fig. S3).

In the structure of the ligand-bound AtFAAH, the C_{18} substrate analogue MLnFP was located in a long, deep pocket, which defines the AtFAAH acyl-binding channel (ABC) (Figs. 4-6 and S4). The entrance of the ligand-binding pocket is composed of a set of hydrophobic amino acids (Ala²⁷, Pro²⁸, Leu³⁰, Phe³⁸, Ile⁵¹, and Leu⁵⁵) and two charged residues (Lys²⁶ and Asp⁵⁸) on α -helices α 1 and α 2 of the unique N-terminal region. This arrangement suggests that hydrophobic ligands access the active site through the membrane cap, which may itself be regarded as a component of the entrance channel (Fig. 3). By contrast, the putative substrate entry site of the rat FAAH is formed with hydrophobic residues on helices α 18 and α 19 and

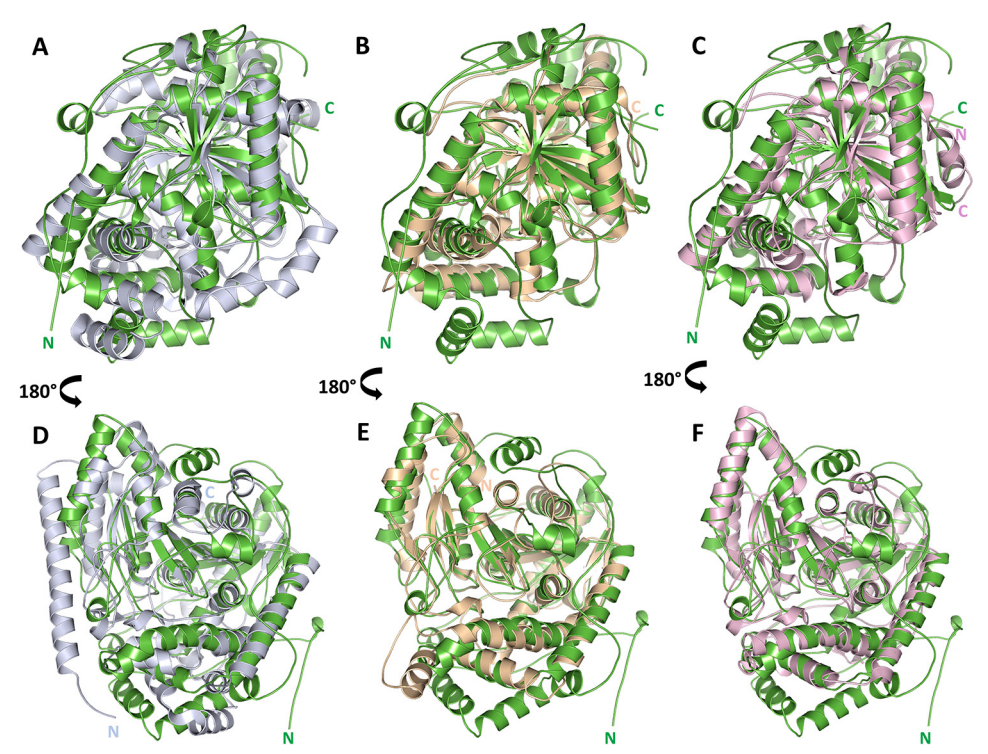


Figure 2. Comparison of Arabidopsis FAAH structure with other AS enzymes. A-F, AtFAAH (green; PDB code 6DHV) was superposed to the structures of rat FAAH (gray; PDB code 3QJ8 (14)) (A and D), glutamine amidotransferase subunit A (wheat; PDB code 3KFU (15)) (B and E), and aryl acylamidase (pink; PDB code 4YJ6 (18)) (C and F) and presented as structure overlays from two different views. The N and C termini of each enzyme are indicated with letters of the same color as the corresponding protein structure.

charged residues Arg^{486} and Asp^{403} , and this alters the position of the membrane access channel (MAC) relative to the interior core of the substrate-binding pocket (Figs. 5 and S3).

The AtFAAH substrate-binding pocket is mostly hydrophobic, formed with amino acids from the N-terminal long loop (Met²⁵ and Ala²⁷), and $\alpha 2-3$ (Leu⁵⁵, Asn⁵⁹, and Met⁶¹), $\alpha 17$ (Val⁴⁴² and Ile⁴⁴⁵), $\alpha 18$ (Ser⁴⁷², Ile⁴⁷⁵, Phe⁴⁷⁶, and Phe⁴⁷⁹), $\alpha 21$ (Ile⁵³², Thr⁵³⁵, Thr⁵³⁶, and Met⁵³⁹), Met²⁵⁶, and Thr²⁵⁸ (Fig. 4). These residues define a long ABC, with the portion near the entrance regarded as the MAC. The MLnFP acyl chain primarily engages in van der Waals interactions with the hydrophobic residues in the ABC (Fig. 4). Notably, several hydrophilic residues (Asn⁵⁹, Thr²⁵⁸, His⁴⁴¹, Ser⁴⁷², Thr⁵³⁵, and Thr⁵³⁶) also are present in the substrate-binding pocket (Fig. 4). This feature results in an ABC that is considerably more polar than that of rat FAAH (Fig. 5, E and F) and endows the AtFAAH ABC the capacity to interact with a diverse array of aliphatic substrates without or with polar functional groups. Primary sequence comparisons of higher plant and mammalian FAAHs showed that a subset of these polar residues are conserved only in higher plant FAAHs, whereas hydrophobic substituents are conserved in the mammalian enzymes (Fig. S5). The active site is located deep in the bottom of the long substrate-binding pocket, and the phosphorus atom of the inhibitor MLnFP is covalently bonded to the catalytic nucleophile, Ser³⁰⁵ (Figs. 4 and 5E). Ser³⁰⁵, Ser²⁸¹, and Lys²⁰⁵ form the catalytic triad in the AtFAAH active site, similar to rat FAAH and other AS enzymes. These findings are consistent with previous site-directed mutagenesis studies that demonstrated key catalytic roles for these residues (20).

AtFAAH dimer formation involves a network of hydrogen bonds and van der Waals interactions contributed by several amino acid residues located at the interface between both subunits. Specifically, residues from the long loop region of the N terminus (Gln⁵, Arg⁶⁶, Thr⁶⁸, and Phe⁷⁶), α 17 (Thr⁴⁵⁴ and Pro^{455}), $\alpha 20$ (Phe⁴⁷⁹ and Ala⁴⁸¹), and Asp^{225} primarily form the oligomerization domain in AtFAAH (Fig. 7). Although different regions of the protein contribute to dimer formation in Arabidopsis and rat FAAHs, both enzymes assume a symmetric pattern of dimerization that aligns the protein subunits in a similar orientation so that the membrane-binding cap and the membrane access channel of each subunit are placed on the same face of the dimer (Fig. 1). Such parallel monomer orientations should enhance membrane binding and allow both subunits to function concurrently.

Unique characteristics of AtFAAH ABC and MAC

The AtFAAH substrate-binding pocket is more open and relatively more polar than that of rat FAAH (Figs. 5 and 6). In rat FAAH, there are two distinct channels for substrate access and acyl chain binding with two hydrophobic residues (Phe432 and Trp⁵³¹) forming the so-called "dynamic paddle" located at the junction of these two regions (Figs. 5D and 6B). In AtFAAH, there are no residues that correspond to Phe⁴³² and Trp⁵³¹, and the substrate is presumed to access directly from the membrane to the acyl chain-binding channel. That is, the MAC and ABC in AtFAAH are not separate structural elements but rather one long access channel (Figs. 5C and 6A). Moreover, a detailed comparison of several selected residues lining the substratebinding pockets of AtFAAH and rat FAAH (Fig. 5, E and F)



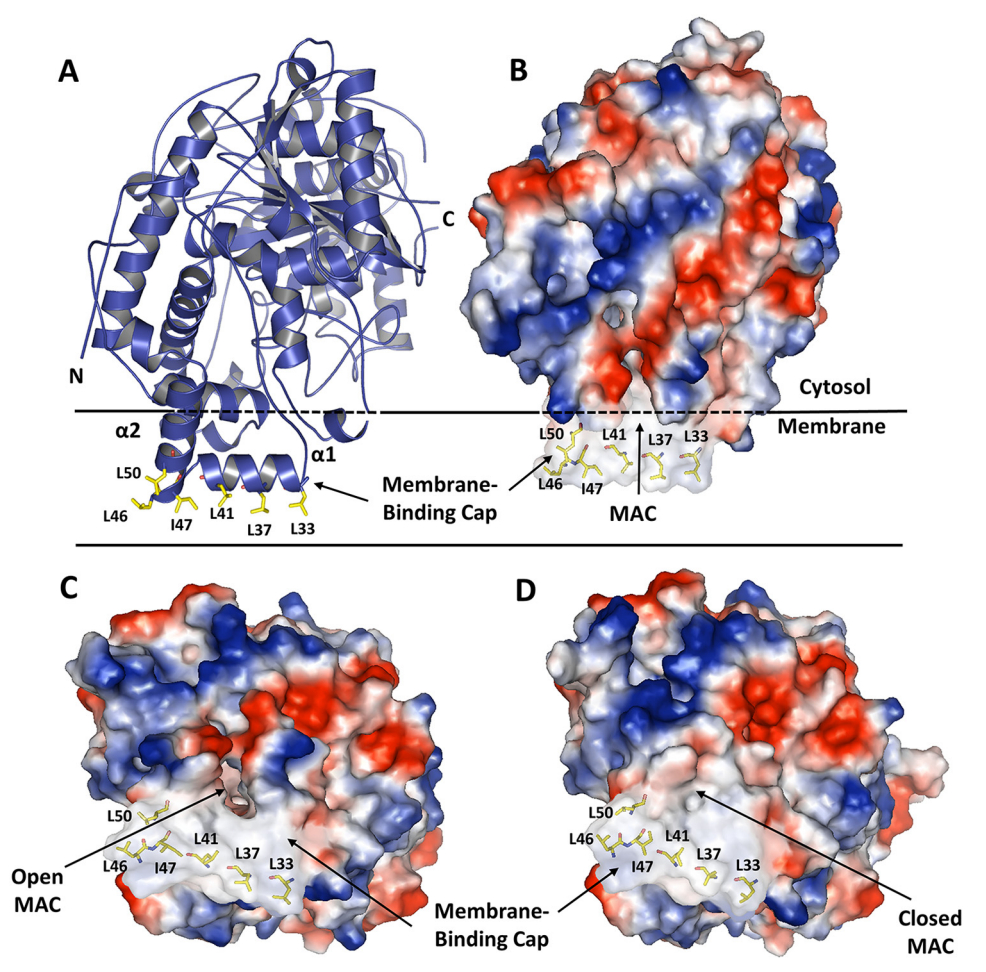


Figure 3. The putative membrane-binding cap of AtFAAH. The hydrophobic helices α 1 and α 2 of the N terminus (amino acids 27–60) are rich in hydrophobic amino acids (21 of 34) and are predicted to form the membrane-binding cap of AtFAAH that is presumed to anchor the enzyme into half of the lipid bilayer. *A* and *B*, one monomer of apo-AtFAAH (PDB code 6DHV) integrated into the membrane is shown in both cartoon (*A*) and electrostatic surface (*B*) depictions with positive charged areas in *blue*, negative charged areas in *red*, and hydrophobic areas in *white*. *C* and *D*, electrostatic molecular surface of AtFAAH viewed from the membrane face showing the membrane-binding cap and the MAC in the open (*C*) and closed (*D*) conformations in apo- (PDB code 6DHV) and MLnFP-bound (PDB code 6DII) AtFAAHs, respectively. Some of the hydrophobic amino acids on helices α 1 and α 2 are highlighted as *yellow sticks* with their numbers and single-letter codes indicated.

revealed substantial structural differences between the plant and rat enzymes. Although both substrate-binding pockets are lined with aliphatic and aromatic amino acids that surround and interact with the acyl chain of the substrate, the AtFAAH substrate-binding pocket has several polar residues not present in rat FAAH (*e.g.* Ser⁴⁷² *versus* Leu⁴⁰⁴ and Thr²⁵⁸ *versus* Phe¹⁹⁴ as well as other polar residues in AtFAAH such as Thr⁵³⁵) (Figs. 5, *E* and *F*, and S5). Overall, the more open and polar substrate-binding pocket of AtFAAH suggests a molecular rationale for its ability to accommodate "bulkier" oxylipin substrates.

AtFAAH accommodates NAE oxylipins

The 9-LOX metabolite of NAE 18:2 (acylethanolamide with 18 carbons and two double bonds in the acyl chain) (Fig. 8, *A* and *B*) is the bioactive molecule that interacts with abscisic acid signaling to invoke a so-called secondary dormancy in *Arabidopsis*. This response is a survival mechanism that enables seedlings to arrest growth under unfavorable environmental conditions (3). We considered the possibility that AtFAAH hydrolyzes both oxylipin and unsubstituted NAE substrates to regulate NAE signaling. To determine whether AtFAAH

hydrolyzes NAE oxylipins, enzyme kinetic studies and computational docking experiments were performed (Fig. 8, *C*–*F*). Initial velocities were measured for recombinant AtFAAH (Fig. 8C) and rat FAAH (Fig. 8D) as a function of increasing concentrations of either [1-14C]NAE 18:2 or [1-14C]NAE-9-HOD. Indeed, AtFAAH hydrolyzed 9-hydroxy-10,12-octadecadienoylethanolamide (NAE-9-HOD) with equal or better catalytic efficiency than the enzyme hydrolyzed NAE 18:2. By contrast, the ethanolamide oxylipin was a decidedly inferior substrate for rat FAAH when measured against the unsubstituted NAE. This in vitro enzymatic activity of AtFAAH toward NAE-9-HOD is consistent with previous findings that AtFAAH overexpressors and knockout mutants accumulated lower and higher levels of endogenous NAE-9-HOD, respectively, and that seedlings of AtFAAH overexpressors were tolerant to the root growthinhibiting effect of exogenous NAE-9-HOD (3). Moreover, docking experiments with NAE-9-HOD in the substrate-binding pocket of AtFAAH revealed that the acyl chain of the substrate can assume two distinct energetically favorable poses in the active site (Fig. 8F). Specifically, molecular dynamics (MD) simulation of the AtFAAH-NAE-9-HOD complex visualized a

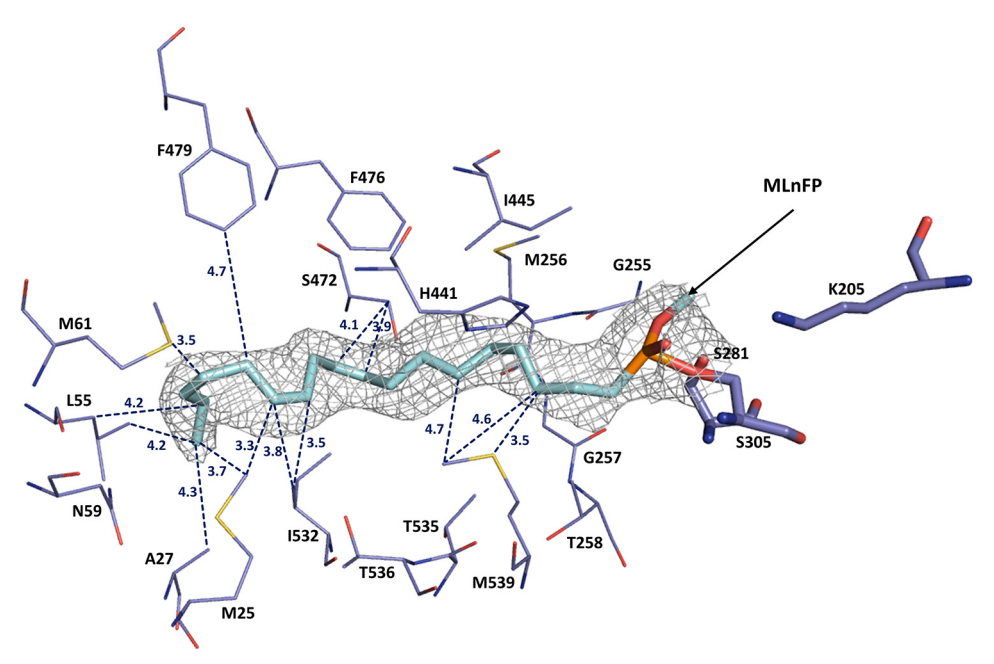


Figure 4. Arabidopsis FAAH active site and substrate-binding pocket. The acyl chain of the irreversible inhibitor MLnFP (cyan sticks) is surrounded by several aliphatic and aromatic amino acids as well as some polar residues (e.g. Asn⁵⁹, Thr²⁵⁸, His⁴⁴¹, Ser⁴⁷², Thr⁵³⁵, and Thr⁵³⁶). All the depicted residues (slate blue lines) are within 5-Å distance from the inhibitor. Representative van der Waals interactions between the ligand and some of the surrounding residues are shown as blue dashed lines with the distance of each potential interaction indicated; only a few selected interactions are shown for simplification. The Ser³⁰⁵-Ser²⁸¹-Lys²⁰⁵ catalytic triad is shown (slate blue sticks) with the nucleophilic Ser³⁰⁵ covalently bound to the phosphorus atom of MLnFP. The $2F_0 - F_0$ electron density map of MLnFP contoured at 1.0 σ is shown in gray.

transition in the binding of NAE-9-HOD between these two poses with the 9-hydroxyl group interacting with either Ser⁴⁷² or Thr⁵³⁵ (Movie S1). The identification of a potential hydrogen bonding interactions of the oxylipin ligand with the side-chain oxygen of either Ser⁴⁷² or Thr⁵³⁵ was consistent with the theoretical possibility that AtFAAH accommodates the binding of NAE oxylipins.

Conformational changes upon ligand binding

Determination of AtFAAH structures without and with bound ligand identified three discrete sets of conformational changes in AtFAAH that accompanied ligand binding. First, the movement of amino acids 25-28 that form one side of the MAC, as well as movement of Leu⁵⁵ on the opposite side of the MAC, resulted in MAC closure upon ligand binding (Fig. 9). Second, a conformational rotation of the Asn⁵⁹ side chain had the dual effects of extending the substrate-binding pocket to support ligand binding and contributing to MAC closure (Fig. 9). These gating residues in AtFAAH (especially Ala²⁷, Pro²⁸, Leu⁵⁵, and Asn⁵⁹) are conserved in sequences of other higher plant FAAH enzymes (Fig. S2). The third set of discrete conformational changes involved the 531–537 region of helix α 21, which shifted toward, and interacted with, the bound ligand. Particularly prominent in that regard were residues Ile⁵³², Thr⁵³⁵, and Thr⁵³⁶, all of which contribute to the AtFAAH ABC (Fig. 9).

These collective conformational changes in AtFAAH "squeeze and lock" the substrate into the binding pocket for hydrolysis. Consistent with this idea, comparison of solventaccessible surface areas (SASA) and cavity volumes of "apo" and ligand-bound conformations indicated that there were approximately 8 and 16% reductions in SASA and substrate cavity

volumes upon ligand binding, respectively. On the contrary, similar calculations for rat FAAH in apo (PDB code 3QJ8 (14)) and inhibitor-bound (PDB code 3QJ9 (14)) conformations showed 15 and 10% increases in SASA and cavity volume, respectively, further suggesting a different mechanism of ligand entry and binding. Indeed, the squeeze and lock mechanism for AtFAAH differs fundamentally from that posited for rat FAAH where Phe⁴³² rotates its side-chain orientation from the ABC to the MAC upon ligand binding and is proposed to guide the substrate toward the active site for hydrolysis (13, 14, 21).

To further dissect the conformational transitions in the MAC and ABC regions of AtFAAH upon ligand binding, allatom MD simulations were carried out. In the AtFAAH apo structure, a partial unfolding of the 531-537 helix region was observed (Fig. 10A and Movie S2). By contrast, that structural element was stabilized and shifted toward the ligand in the AtFAAH-MLnFP bound structure. In that conformation, the 531-537 helix region enclosed the ABC in a manner consistent with the crystal structure (Fig. 10B and Movies S3 and S4). These 531-537 helical region dynamics were analyzed in further detail in two additional sets of independent MD simulations where (i) MLnFP was removed from the cocrystal structure, resulting in derived apo structure and (ii) MLnFP was docked into the apo crystal structure to produce a docked cocrystal structure. In both sets of simulations, the conformational dynamics of this helical region were reproduced (Fig. 10, C and D, and Movies S5 and S6). The presence of this random coil motif in AtFAAH likely confers more plasticity to the substrate-binding pocket, which in turn makes the enzyme more able to accommodate a broader range of substrates. Moreover, a noticeable shift and uncoiling in the N-terminal $\alpha 1$ and $\alpha 2$



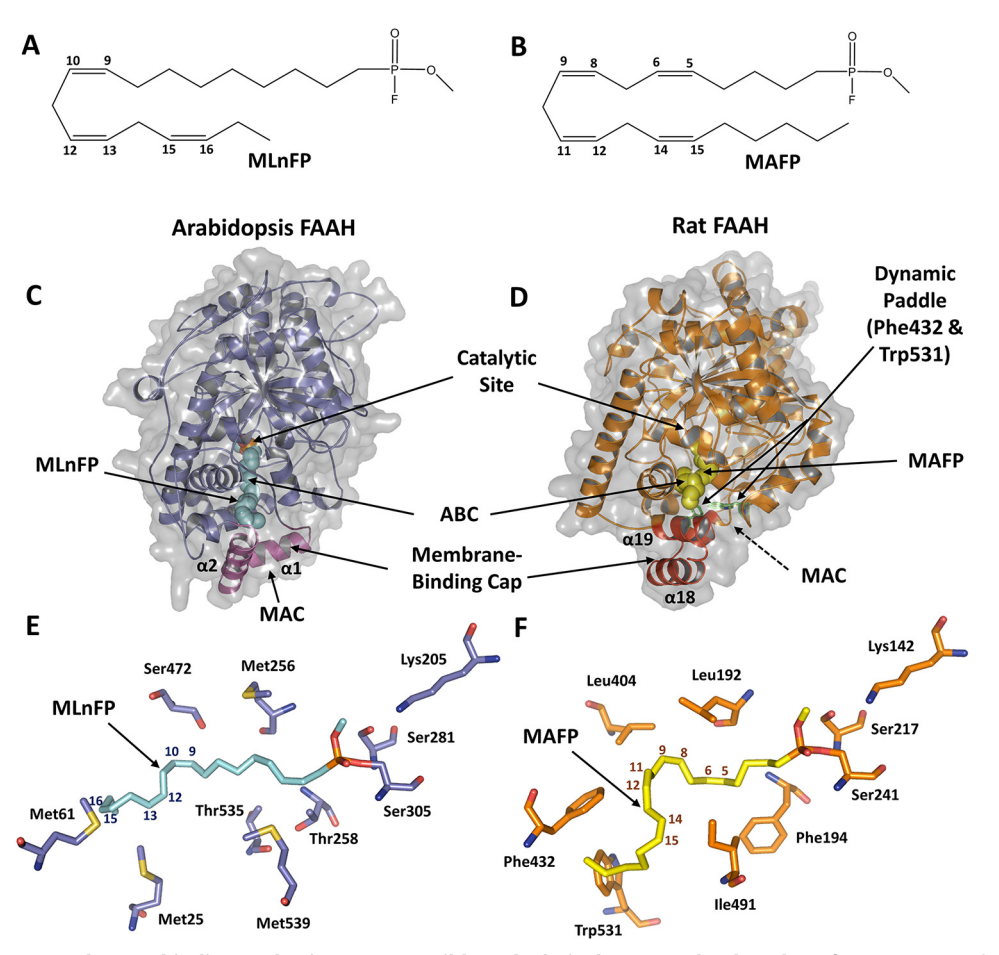


Figure 5. Arabidopsis FAAH substrate-binding pocket is more accessible and relatively more polar than that of rat FAAH. A and B, chemical structures of the irreversible inhibitors MLnFP and MAFP. C and D, one subunit of the ligand-bound AtFAAH (C) (PDB code 6DII) and rat FAAH (D) (PDB code 1MT5) (12) are shown with the protein molecular surface rendered gray and transparent to illustrate the key differences between both enzymes with respect to the MAC and the ABC. The putative membrane-binding cap is colored magenta (α 1 and α 2) and red (α 18 and α 19) in AtFAAH and rat FAAH, respectively. In rat FAAH, the dynamic paddle residues, Phe⁴³² and Trp⁵³¹, are shown as green sticks. E and F, comparison of the substrate-binding pockets of AtFAAH (E) (PDB code 6DII) and rat FAAH (F) (PDB code 1MT5) complexed with MLnFP (cyan sticks) and MAFP (yellow sticks), respectively. Both enzymes were superposed, and the substrate-binding pockets were compared; only a few selected residues are shown for simplification. The amino acid residues of AtFAAH are shown as slate blue sticks, whereas those of rat FAAH are shown as orange sticks. The numbers on the ligands indicate the position of the double bonds.

helices was also observed in these MD simulations (especially in the absence of ligand; Fig. 10, *A* and *C*), suggesting that concerted movements of these key regions in the MAC and ABC are required to accommodate ligand binding.

Conclusions

Taken together, our results outline the structural organization of AtFAAH that supports its efficient activity toward a range of acylethanolamides that include oxygenated derivatives. Our data project that this is a result of a "malleable," easily accessible, and relatively more polar substrate-binding pocket that supports a squeeze and lock substrate-binding mechanism (Fig. 11A). This is fundamentally distinct from the case for rat FAAH that is proposed to consist of discrete membrane access and substrate-binding channels and requires a conformational "flip" of dynamic paddle residues to correctly orient the substrate for catalysis (Fig. 11B). Moreover, these results add new structural and functional information to the family of amidase signature enzymes more broadly and provide a mechanistic explanation for the structural divergence of acylethanolamide signaling in plants and endocannabinoid signaling in mammals.

The utilization of NAEs as signaling molecules is a common feature of most, if not all, multicellular organisms (9). The formation and turnover of this group of lipids are broadly conserved across animal and plant kingdoms, particularly with regard to signal termination by the action of FAAH (6). Herein, we identify the structural differences in the signal-terminating enzyme AtFAAH that facilitate the efficient hydrolysis of ethanolamide oxylipins. This diversification in ligand specificity represents an important evolutionary adaptation of NAE signaling in higher plants. These collective results not only support an expanded view of NAE signaling beyond that of the intensively studied endocannabinoid pathway of mammals but also support the concept that oxylipin derivatives of NAEs have important signaling functions with activities that are terminated by FAAH enzymes in higher plants.

FAAH recently was suggested to play a key role in plant responses to a class of bacterial quorum-sensing signals, namely *N*-acyl L-homoserine lactones (AHLs). FAAH hydrolysis of AHLs was shown to be pivotal for plants to perceive these quorum-sensing signals and hence mediate plant–microbe interactions (22, 23). These studies emphasized the concept

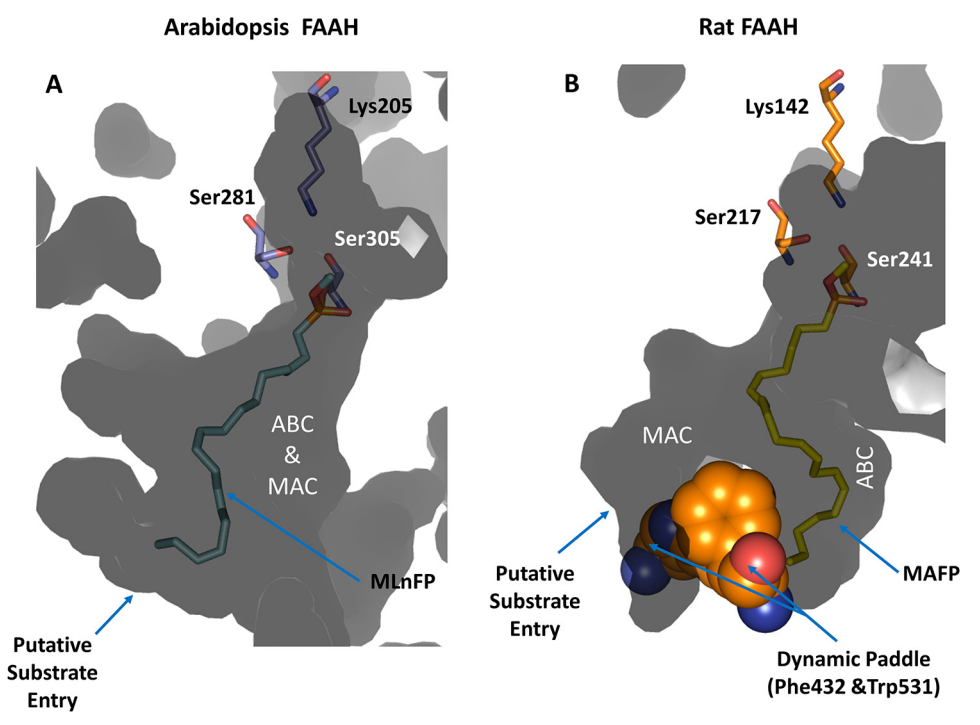


Figure 6. Differences in the organization of the MAC and the ABC between Arabidopsis and rat FAAH. A and B, one subunit of the ligand-bound Arabidopsis FAAH (A) (PDB code 6DII) and rat FAAH (B) (PDB code 1MT5) (12) were superposed, and their cavities/channels are shown as dark gray shadows. In rat FAAH, there are two distinct channels for substrate access and acyl chain binding with two hydrophobic residues (Phe⁴³² and Trp⁵³¹; shown in orange, space-filling representation) forming the so-called dynamic paddle located at the junction of these two channels. In Arabidopsis FAAH, there are no residues corresponding to Phe⁴³² and Trp⁵³¹, and the substrate is presumed to access directly from the membrane to the acyl-binding channel. In other words, in AtFAAH, there is only one large cavity for both substrate access and binding (i.e. indistinguishable MAC and ABC). The catalytic triad residues are shown as slate blue and orange sticks in Arabidopsis and rat FAAHs, respectively. The irreversible inhibitors MLnFP (cyan sticks) and MAFP (yellow sticks) are shown bound to the active site of Arabidopsis and rat FAAHs, respectively.

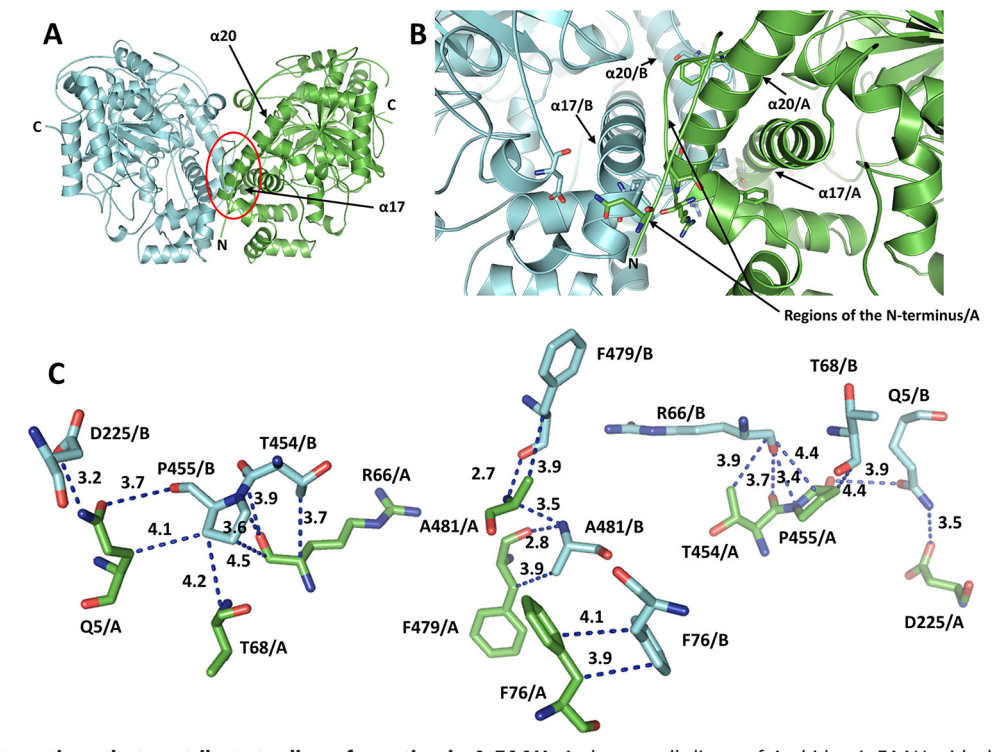


Figure 7. Atomic interactions that contribute to dimer formation in AtFAAH. A, the overall dimer of Arabidopsis FAAH with the dimerization region indicated by a red circle. B, a closeup view of this dimerization region with some of the key residues depicted as sticks; the AtFAAH dimer interface is formed mainly by parts of helices α 17 and α 20 and some loop regions of the N terminus. *C*, detailed representation of the network of hydrogen bonds and van der Waals interactions at the monomer–monomer interface of AtFAAH. Residues from one subunit (chain A) are shown as *green sticks*, whereas those from the other subunit (chain B) are shown as cyan sticks. The single-letter code and the number of each amino acid as well as the distance of each potential interaction are indicated.



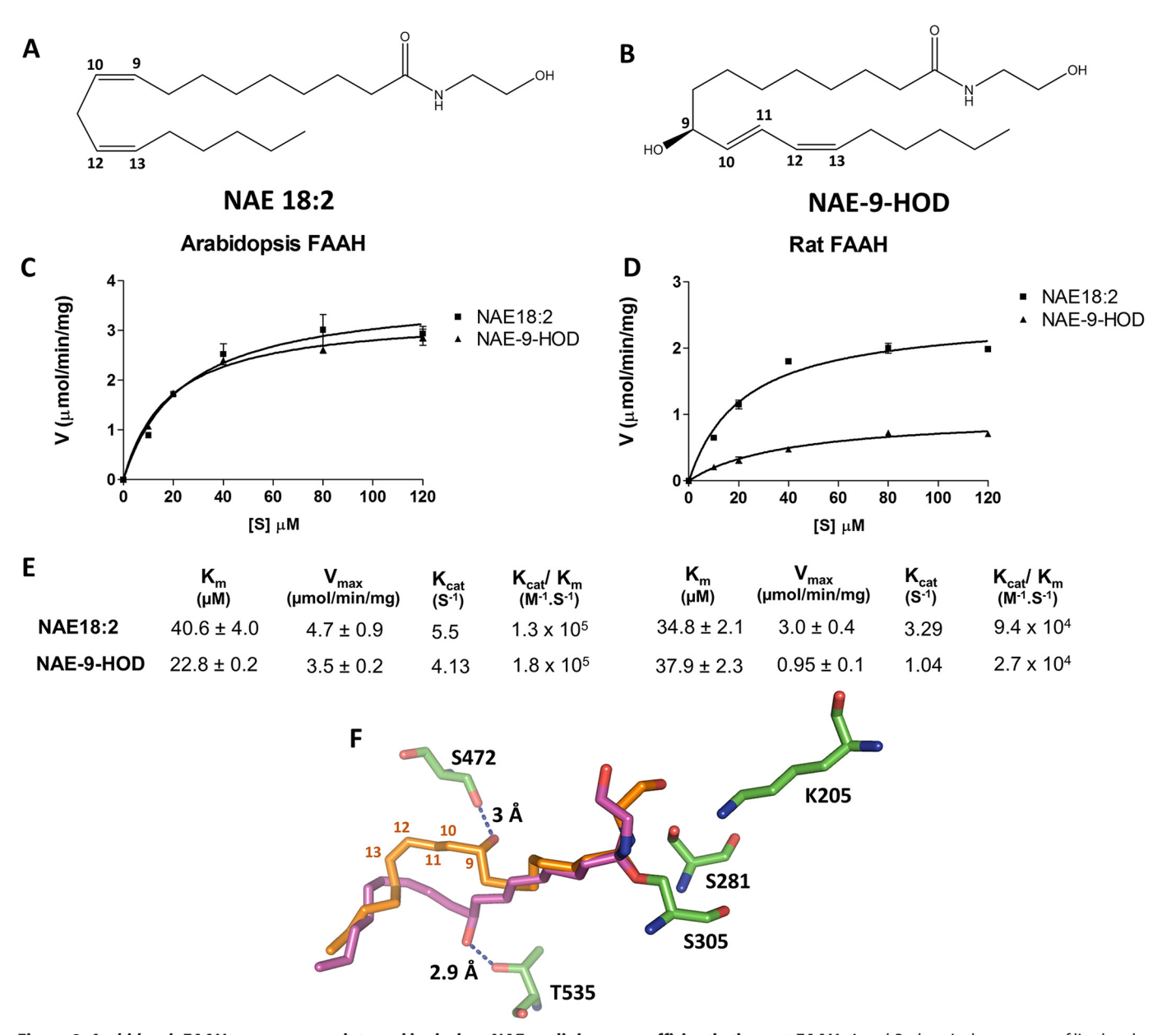


Figure 8. Arabidopsis FAAH can accommodate and hydrolyze NAE oxylipins more efficiently than rat FAAH. A and B, chemical structures of linoleoyle-thanolamide (NAE 18:2) and NAE-9-HOD. C and D, initial velocities were measured for AtFAAH (C) and rat FAAH (D) with increasing concentrations of either [1- 14 C]NAE 18:2 or [1- 14 C]NAE-9-HOD. Data points represent means \pm S.D. (error bars) of triplicate enzymatic assays. E, summary of the apparent kinetic parameters of both enzymes. F, docking of NAE-9-HOD in the substrate-binding pocket of AtFAAH with the oxygenated acyl chain of the substrate displayed in two different binding poses with pose 1 shown as orange sticks and pose 2 shown as magenta sticks. Arabidopsis FAAH amino acid residues are depicted as green sticks. In AtFAAH, Ser⁴⁷² is well-positioned to accommodate and form a hydrogen bond interaction with the hydroxyl group at position 9 when the NAE-9-HOD acyl chain exhibits binding pose 1, whereas Thr⁵³⁵ on the opposite side of the substrate-binding pocket can form a hydrogen bond with the 9-hydroxyl group when the substrate is in binding pose 2 (see Movie S1). The numbers of the ligand atoms (9–13) are indicated for clarity.

that AtFAAH can utilize a broad range of substrates, which is consistent with our structural findings with respect to the openness and flexibility of the AtFAAH substrate-binding pocket. The AtFAAH structure presented here will form the basis for future studies to understand how plant FAAHs recognize and utilize AHLs as substrates and to explore the diversity of FAAH-like enzymes in various plant species.

Experimental procedures

Arabidopsis FAAH protein expression and purification

Recombinant AtFAAH (At5g64440; UniProt accession number Q7XJJ7) was expressed in *E. coli* TOP10 cells from the

pTrcHis2 plasmid as described previously (24) with a few modifications in expression, enzyme extraction, and purification to support crystallization studies. Overnight cultures grown in LB medium containing 100 μ g/ml ampicillin (37 °C) were inoculated into fresh medium and grown at 37 °C to an OD₆₀₀ of 0.5–0.7. Recombinant protein expression was induced with 1 mM isopropyl β -D-1-thiogalactopyranoside for 20 h at 22 °C. Cells were harvested by centrifugation (4,000 \times g, 10 min, 4 °C) and frozen at -20 °C for at least 24 h. Frozen cells were thawed and suspended in lysis buffer (50 mM Tris-HCl, pH 8.0, 100 mM NaCl, 1% (v/v) Triton X-100) supplemented with 1 mg/ml lysozyme and 25 units/ml Benzonase nuclease (Sigma-Aldrich).



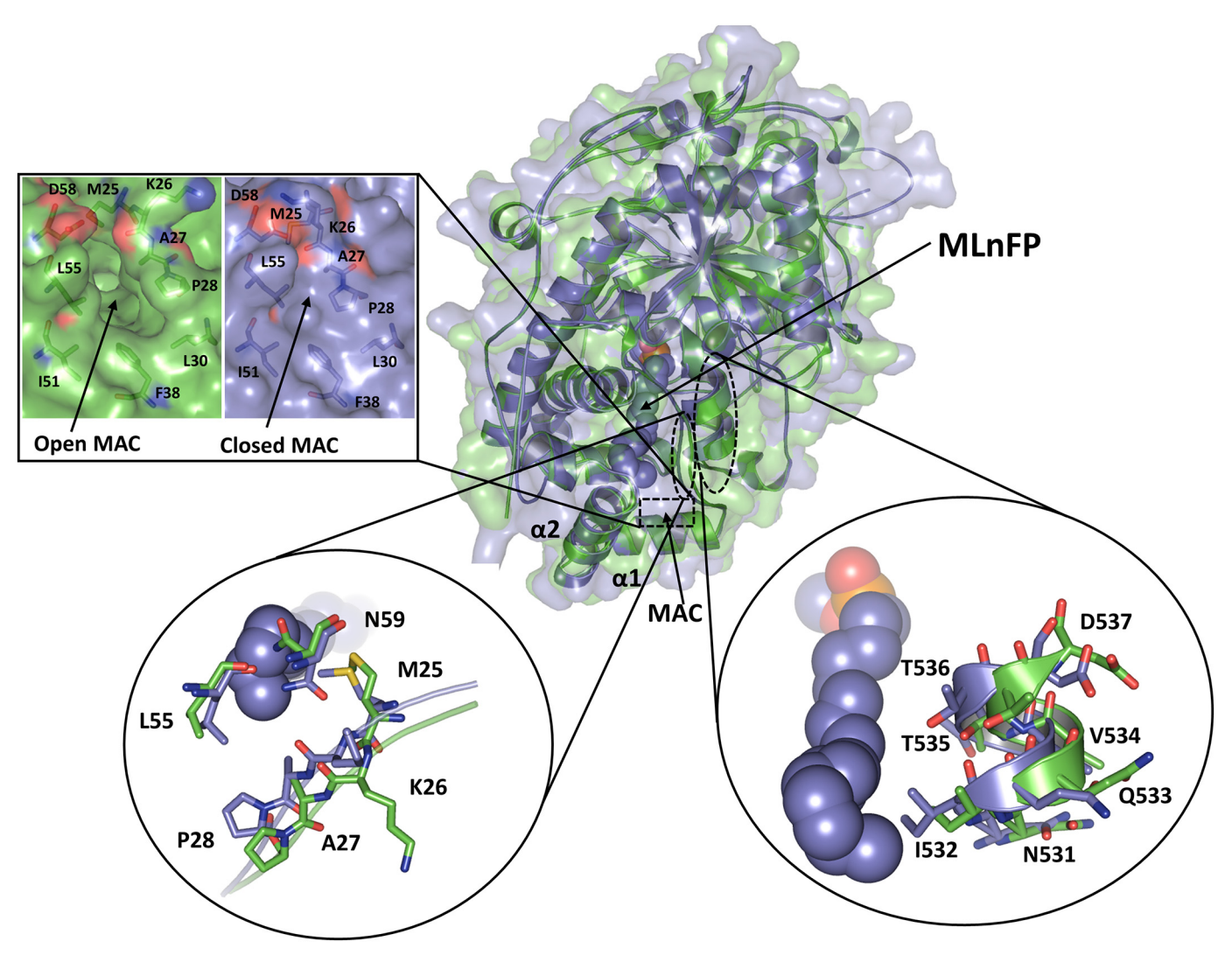


Figure 9. Conformational changes in Arabidopsis FAAH structure upon ligand binding. The superposed structures of one subunit of AtFAAH in both the apo (green; PDB code 6DHV) and ligand-bound (slate blue; PDB code 6DII) forms are shown. The ligand MLnFP is depicted as blue spheres. Regions of the protein that undergo conformational changes are enlarged to demonstrate the details of each group of changes. The zoomed-in surface region is a closeup view of the protein molecular surface from the membrane face showing the open (green) and closed (slate blue) MAC in the apo- and MLnFP-bound AtFAAHs, respectively; the protein surface was rendered partially transparent to show the corresponding amino acid residues.

After incubation on ice for 30 mins, cells were sonicated on ice with 15 30-s bursts at 50% intensity with a 30-s cooling period between bursts (Microson MS-50 Ultrasonic Cell Disruptor; 50 watts). The crude lysate was centrifuged at $14,000 \times g$ for 45 min at 4 °C, and the supernatant was loaded onto nickel-nitrilotriacetic acid-agarose beads (Qiagen). The beads were successively washed with three wash buffers of increasing imidazole and DDM concentrations to elute nonspecific proteins and to exchange detergents: 1) 50 mm Tris-HCl, pH 8.0, 500 mm NaCl, 1% (v/v) Triton X-100, 10 mm imidazole; 2) 50 mm Tris-HCl, pH 8.0, 500 mm NaCl, 1% (v/v) Triton X-100, 25 mm imidazole; and 3) 50 mm Tris-HCl, pH 8.0, 500 mm NaCl, 0.01% (w/v) DDM, 40 mm imidazole. Finally, recombinant His-tagged proteins were eluted with 50 mm Tris-HCl, pH 8.0, 500 mm NaCl, 0.03% DDM, 250 mm imidazole and concentrated using Amicon Ultra 30,000 centrifugal filter devices (Millipore, Bedford, MA) with the buffer exchanged to BTP buffer (50 mm Bistris propane, pH 9.0, 100 mm NaCl, 0.03% (w/v) DDM). Purified recombinant FAAH protein was fractionated by size-exclusion

FPLC (Amersham Biosciences) using Superdex 200 Increase 10/300 GL columns (GE Healthcare). The column was equilibrated with BTP buffer, and the eluted proteins were monitored by UV absorbance at 280 nm. Arabidopsis FAAH was eluted in two size fractions (of about 200 and 400 kDa) compared with molecular mass standards. FAAH was confirmed to be in these fractions by SDS-PAGE analysis and enzyme activity assays. Only the AtFAAH fractions in the 200-kDa range (Fig. S1; fraction 2) were collected, concentrated as above, aliquoted, flash frozen in liquid nitrogen, and stored at -80 °C until use. The molecular mass calibration of the column was performed using a commercially available gel filtration standard (Bio-Rad), which is a mixture of molecular mass markers ranging from 1,350 to 670,000 Da. The concentration of the purified protein was determined by a Pierce BCA protein assay kit (Thermo Fisher Scientific, Rockford, IL). High yields of the full-length AtFAAH (5-7 mg of purified protein/liter of culture) enabled a large number of crystallization experiments.



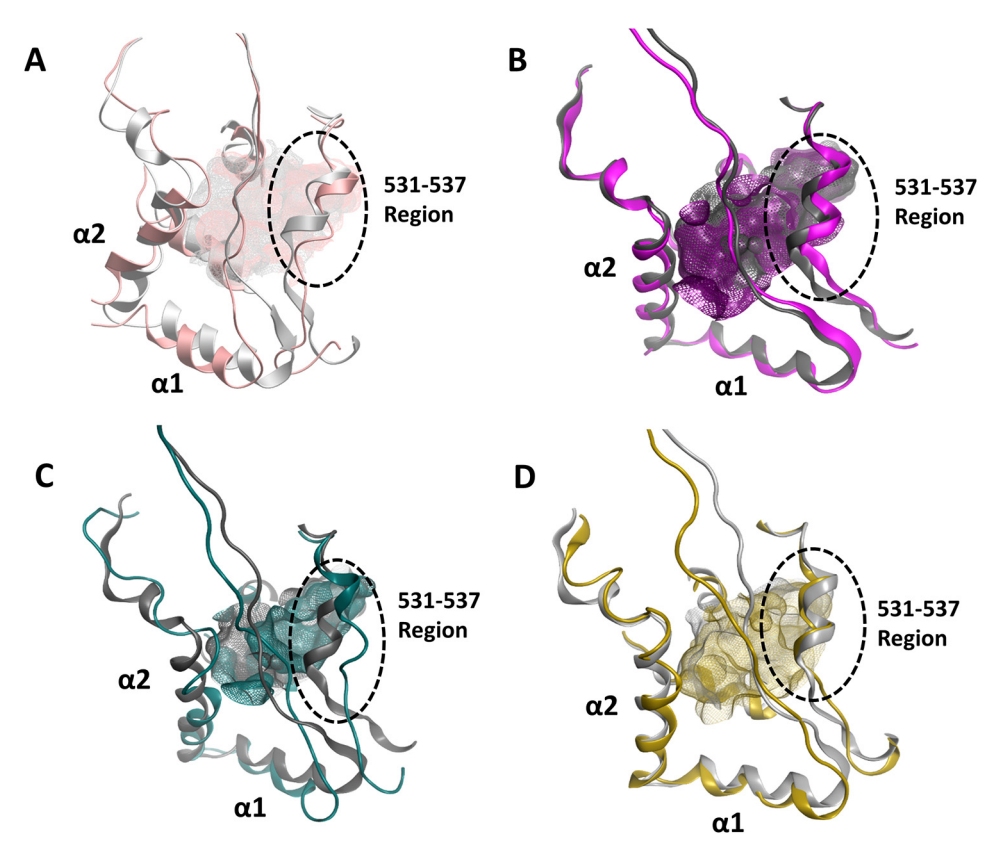


Figure 10. Molecular dynamics simulations of Arabidopsis FAAH. A, overlay of the first ($light\ gray$) and last (pink) frames of a 100-ns MD simulation of the apo-AtFAAH structure (see Movie S2). B, overlay of the first ($dark\ gray$) and last (magenta) frames of a 100-ns MD simulation of the MLnFP-bound structure (see Movie S4). C, the ligand MLnFP was removed from the bound cocrystal structure, and the resulting apo structure was simulated for 100 ns (see Movie S5); the first and last frames are shown in $dark\ gray$ and teal, respectively. D, MLnFP was docked into the apo-AtFAAH structure, and the resulting AtFAAH-MLnFP complex was simulated for 100 ns (see Movie S6); the first and last frames are shown in $light\ gray$ and $golden\ yellow$, respectively. $ln\ A$ and C, partial unfolding of the 531-537 helix region and noticeable shifts in the N-terminal α 1 and α 2 helices were observed in the absence of the ligand, whereas in B and D, these changes were not observed in the presence of MLnFP. The $mesh\ rendering\ indicates\ the\ surface\ of\ the\ cavity.$

Arabidopsis FAAH protein crystallization

The purified AtFAAH protein was initially screened by the sparse-matrix method (25) using the crystal screen kits from Qiagen at 20 °C by sitting drop vapor diffusion with a Phoenix crystallization robot (Art Robbins Instruments, Sunnyvale, CA). Protein sample (20-25 mg/ml) was mixed with an equal volume of reservoir solution, and the mixture was equilibrated over the reservoir solution. Crystals of AtFAAH were obtained after extensive screening (800 different conditions). Crystallization was optimized further by hanging drop vapor diffusion where larger, high-quality AtFAAH crystals were obtained in hanging drops formed of 1 μ l of concentrated protein (25 mg/ml) and 1 μ l of reservoir solution (0.1 M MES buffer, pH 6.0, 30% PEG 200, 5% PEG 3350) at 20 °C. For the ligand-bound AtFAAH, crystals were obtained by cocrystallization under the same conditions, but the irreversible inhibitor MLnFP (Cayman Chemical, Ann Arbor, MI) was dissolved in DMSO and added to the reservoir solution to achieve a final protein-toligand molar ratio of 1:5.

X-ray diffraction data collection

X-ray diffraction data sets were collected for ligand-free (apo form) and ligand-bound AtFAAH crystals at 2.1 and 3.2 Å, respectively, at beamline 14-1 of the Stanford Synchrotron Radiation Lightsource. The data were processed by the program HKL2000

(26). Both crystals belonged to the space group $P2_1$ but with different unit cell parameters: for apo-AtFAAH, a=72.08 Å, b=79.66 Å, c=132.59 Å, $\beta=104.4^\circ$; whereas for ligand-bound AtFAAH, a=225.57 Å, b=83.31 Å, c=272.81.59 Å, $\beta=110.98^\circ$. The calculated Matthews coefficients ($V_M=2.5$ Å 3 Da $^{-1}$) (27), corresponding to a solvent content of 50%, indicated the presence of two and 12 molecules in the asymmetric unit for apo- and ligand-bound AtFAAH, respectively.

Structure determination and refinement

For structure determination of apo-AtFAAH, molecular replacement studies were carried out with the program Phaser (28), and a good solution was obtained with the transamidosome structure (PDB code 3KFU) (15) as a search model. Interactive model building was carried out with the program Coot (29). Crystallographic structure refinements were performed using the programs Refmac (30) and PHENIX (31). The B-factors were refined individually. Water molecules were added with PHENIX and checked manually for inclusion. The high resolution and good quality of the electron density map allowed for model building of all the amino acids except a small gap at 118–125 where the poor electron density in this region did not allow for model building of these eight amino acids (probably a disordered or flexible region in the apo-AtFAAH structure). Other missing residues in the structure include the first three



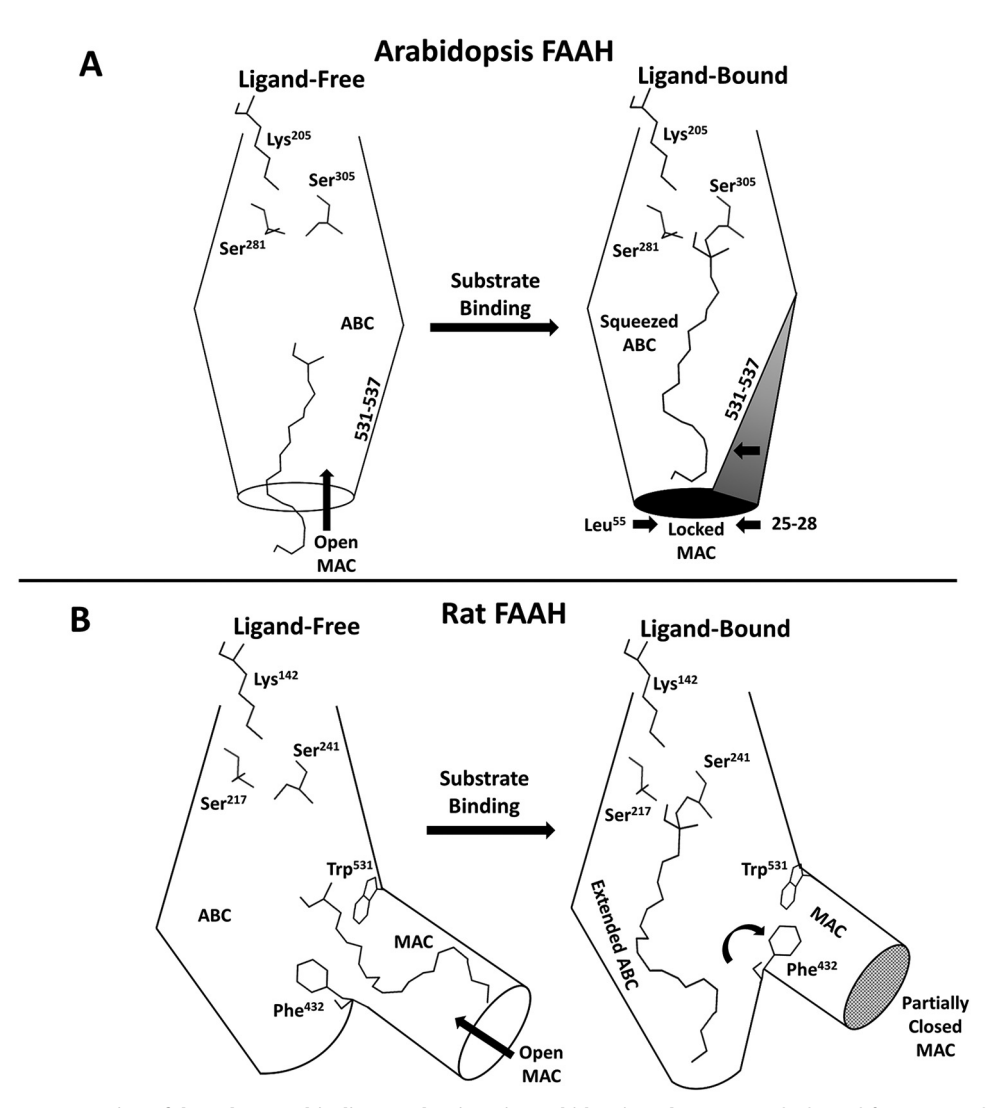


Figure 11. Schematic representation of the substrate-binding mechanisms in Arabidopsis and rat FAAH. The liqand-free AtFAAH has a long, widely open ABC with the part near the entrance regarded as the MAC. Ligand binding triggers movement of the 531-537 helix region of the ABC toward the substrate, resulting in a "squeezed" ABC. This is accompanied by a concomitant movement of residues 25–28 as well as Leu⁵⁵, located on the opposite sides of the MAC, resulting in a "locked" MAC. These changes in AtFAAH upon ligand binding squeeze and lock the substrate into the binding pocket for hydrolysis. By contrast, rat FAAH has two separate acyl-binding and membrane access channels. In the absence of ligand, the dynamic paddle residue Phe⁴³² is oriented toward the ABC, resulting in a short ABC and a long, open MAC. Upon ligand binding, Phe⁴³² changes its side-chain orientation from the ABC to the MAC, resulting in an extended ABC and partially closed MAC. This conformational flip of the dynamic paddle residue is proposed to guide the substrate toward the active site for hydrolysis (13, 14, 21).

amino acids at the N terminus of one subunit (chain A) and the last two amino acids at the C terminus of both subunits. The program PROCHECK (32) was utilized to check the model, and all backbone ϕ - ψ torsion angles are within the allowed regions of the Ramachandran plot.

For ligand-bound AtFAAH, a good molecular replacement solution was obtained by using the apoenzyme dimer structure as a search model. Model building and refinement were carried out with the same programs. In this case, the structure model has six dimers in the asymmetric unit. All amino acid residues were modeled into the electron density map except the first three amino acids in chains A, C, E, G, I, and K and the last two amino acids in chains A-G, I, and K. Three chains (H, J, and L) had an additional map at their C termini, most likely corresponding to some sequence from the plasmid (pTrcHis2), so about nine additional amino acid residues were modeled into these regions. All amino acids are within the allowed regions of

the Ramachandran plot. The small-molecule MLnFP model was built using the methyl arachidonyl fluorophosphonate (MAFP) from the rat FAAH structure (PDB code 1MT5) (12) as a template and manually fitted into the electron density map found in the substrate-binding pocket of AtFAAH. The ligand chemical restraints were generated and geometry-optimized with the programs REEL (33) and eLBOW (34) in PHENIX. A summary of the data collection and refinement statistics is provided (Table S1).

Rat FAAH protein expression and purification

The recombinant plasmid rat FAAH1::pTrcHis2 (NCBI accession number NP_077046) was provided by Dr. Benjamin Cravatt's laboratory (35) and was introduced into E. coli TOP10 cells. To compare the kinetic behavior of *Arabidopsis* and rat FAAHs toward NAE 18:2 and NAE-9-HOD, the rat FAAH recombinant protein was purified by the same expression



and purification procedures described above for Arabidopsis FAAH.

FAAH enzyme kinetics

FAAH enzyme assays were conducted with radiolabeled substrates as described previously (36) with some modifications. The [1-14C]NAE 18:2 was synthesized and purified as described (36) and mixed with nonradiolabeled NAE 18:2 (Cayman Chemical) in two different ratios, and the radiospecific activities were used to calculate enzyme activity following radiometric scanning of TLC-separated FAAH reaction products. Two ratios of radioactive to nonradioactive substrates were prepared so that a wide range of substrate concentrations in the final enzymatic reactions could be tested without excessive dilution of the radioactive molecules. In addition, batches of these two NAE 18:2 mixtures (nonradiolabeled + ¹⁴C-labeled) were used to synthesize radiolabeled NAE-9-HOD ([1-¹⁴C]NAE-9-HOD) using a commercial preparation of potato LOX (with 9-LOX activity; Cayman Chemical) and following previously described procedures (11). Quantities of the purified NAE-9-HOD recovered from each reaction were calculated based on the radiospecific activity of the product following TLC separation (radiometric scanning of TLC plates). Parallel reactions were performed with unlabeled NAE 18:2 only and analyzed by GC-MS to confirm the identity of the product (NAE-9-HOD) and evaluate the purity of product yielded from the 9-LOX reactions. The conversion rate of NAE 18:2 to NAE-9-HOD was more than 90% in all reactions. For consistency, all enzymatic assays for both Arabidopsis and rat FAAHs were performed with the same batches of synthetic substrates. FAAH assays were performed in triplicate at increasing substrate concentrations (10–120 μ M) of either [1-¹⁴C]NAE 18:2 or [1-14C]NAE-9-HOD in 0.25 ml of 50 mm Bis-Tris propane-HCl, pH 9.0, 0.2 mm DDM at 30 °C for 5 min with shaking (120 rpm). The reactions were initiated by adding 0.1 and 0.27 μ g of Arabidopsis and rat FAAHs, respectively, and terminated by adding hot isopropyl alcohol (2 ml, 70 °C, 30 min). After cooling to room temperature, lipids were extracted into chloroform, separated by TLC, and analyzed by radiometric scanning as described elsewhere (36). Initial velocity measurements at increasing substrate concentrations were plotted with Prism version 3.0 (GraphPad Software, San Diego, CA) where the data were fitted to a nonlinear regression (curve fit) using a one-site binding (hyperbola) equation. Correlations between actual measurements and the fitted curves were between $R^2 = 0.94$ and 0.98.

Computational docking experiment of NAE-9-HOD

The protein models were prepared using the Protein Preparation Wizard panel in the Schrödinger suite (2017-4, Schrödinger, LLC, New York, NY) (37). The complete structure of AtFAAH was optimized with the OPLS_2005 force field in the Schrödinger suite to relieve all atom and bond strains found after adding all missing side chains and/or atoms. The small-molecule model structure for the compound NAE-9-HOD was prepared and energy-minimized in MOE (2016.08; Chemical Computing Group ULC, Montreal, Canada) (38), and the lowest energy conformation was selected for docking.

Computational docking was carried out using the genetic algorithm-based ligand docking program GOLD 5.2.1 (39). GOLD explores ligand conformations fairly exhaustively and provides limited flexibility to protein side chains. For computational docking, the crystal structure of the apo-AtFAAH was used. The active site was defined by taking the centroid of catalytic residues in the crystal structure as a reference center to define protein-binding site of radius 10 Å around it with the GOLD cavity detection algorithm. GOLD covalent docking was carried out to find diverse poses of the NAE-9-HOD ligand with a covalent bond constraint set between the side-chain oxygen $(O\gamma)$ of the nucleophilic Ser³⁰⁵ and the carbonyl carbon of the ligand. To explore all the possible binding modes, docking was carried out to generate diverse solutions with early termination turned off. All other parameters were set as the defaults. NAE-9-HOD was then docked and scored using the CHEMPLP scoring function within GOLD as it has been found to give the highest success rates for both pose prediction and virtual screening experiments against diverse validation test sets (40).

Determination of SASA and cavity volume

SASA and cavity volume were calculated on the crystal structures of the apo- and ligand-bound AtFAAH. Similarly, for rat FAAH, apo (PDB code 3QJ8 (14)) and inhibitor-bound (PDB code 3QJ9 (14)) conformations were used. A 5-Å distance cutoff around ligand was used for the calculation. SASA of the binding cavity and change in surface area upon ligand binding were calculated with the binding_sasa.py script implemented within the Schrödinger suite (2017-4, Schrödinger, LLC) (37). Cavity volume was calculated using the SiteMap application within Schrödinger suite (2017-4, Schrödinger, LLC) (37).

Molecular dynamics simulation experiments

All-atom MD simulations were carried out for 100 ns on AtFAAH structures. Crystal structures of AtFAAH in apo "open" conformation and in complex with the irreversible inhibitor MLnFP were used to build starting structures for MD simulations. MD simulations were run for 100 ns each using Desmond version 2016-3 of the MD simulation package (41).

Protein preparation and MD simulations were carried out using the Desmond module of Schrödinger version 2016-3 (D. E. Shaw Research, Schrödinger Inc.) with the OPLS-AA force field as defined in Desmond. System Builder within Desmond/Schrödinger was used to generate a solvated system of protein-ligand complex. An orthorhombic box with a 12-Å buffer around the protein-ligand complex was used to generate a periodic box. An all-atom atomistic-scale MD simulation was carried out in a periodic box of explicit water molecules. For water, the TIP3P water model that is compatible with the OPLS-AA parameterization was employed. Simulation was carried out at 300 K at physiological salt concentration of 150 mm NaCl. Counter ions were included to neutralize the total charge of the system. The OPLS-AA all-atom force field was used to describe all molecules. For AtFAAH-MLnFP, a force constraint was used between Ser³⁰⁵ and the phosphorus atom of the MLnFP headgroup to account for covalent bond interaction. The system was relaxed using Maestro's system relaxation protocol before the production run. This includes a multistage



relaxation protocol with two stages of minimization (restrained and unrestrained) followed by five stages of MD runs with gradually diminishing restraints. All MD production runs were carried out at constant temperature and pressure. Long-range electrostatic interactions were estimated using the particle mesh Ewald, whereas bonds involving protons were constrained using the SHAKE algorithm. A 2-fs time step was used throughout the simulation. For the thermostat, the Nosé-Hoover chain method was applied with a relaxation time of 1 ps. Barostat parameters were set according to Martyna-Tobias-Klein with a relaxation time of 2.0 ps with isotropic coupling. A 9-Å cutoff was applied to Lennard-Jones interactions, and the nonbonded list was updated every 1.2 ps. The production run was continued for 100 ns, and snapshots of the coordinates were written out every 1 ps. MD simulations were repeated for n = 3, starting from a random seed for each simulation. The results were analyzed, and plots were generated within Maestro's Simulation Event Analysis and Simulation Interaction Diagram modules.

Data and materials availability

The structures of AtFAAH were deposited in the Protein Data Bank with accession codes 6DHV (without ligand) and 6DII (complexed with ligand).

Author contributions—M. A., X. W., and K. D. C. conceptualization; M. A. and X. W. data curation; M. A. formal analysis; M. A., A. T., and V. A. B. investigation; M. A., X. W., and A. T. visualization; M. A. and A. T. methodology; M. A., X. W., A. T., and K. D. C. writing-original draft; M. A., X. W., A. T., V. A. B., and K. D. C. writingreview and editing; X. W. resources; X. W., V. A. B., and K. D. C. supervision; X. W. validation; V. A. B. and K. D. C. funding acquisition; K. D. C. project administration.

Acknowledgments—We thank staff scientists at the Stanford Synchrotron Radiation Laboratory (SSRL) for assistance with data collection. Use of the Stanford Synchrotron Radiation Lightsource, SLAC National Accelerator Laboratory, is supported by the United States Department of Energy (DOE), Office of Science, Office of Basic Energy Sciences, under Contract DE-AC02-76SF00515. The SSRL Structural Molecular Biology Program is supported by the DOE Office of Biological and Environmental Research and by the National Institutes of Health, National Institute of General Medical Sciences (including Grant P41GM103393). We also thank The Laboratory for Molecular Simulation and High Performance Research Computing at Texas A&M University for software, support, and computer time.

References

- 1. Lucanic, M., Held, J. M., Vantipalli, M. C., Klang, I. M., Graham, J. B., Gibson, B. W., Lithgow, G. J., and Gill, M. S. (2011) N-Acylethanolamine signalling mediates the effect of diet on lifespan in Caenorhabditis elegans. Nature 473, 226 – 229 CrossRef Medline
- 2. Keereetaweep, J., Blancaflor, E. B., Hornung, E., Feussner, I., and Chapman, K. D. (2013) Ethanolamide oxylipins of linolenic acid can negatively regulate Arabidopsis seedling development. Plant Cell 25, 3824-3840 CrossRef Medline
- 3. Keereetaweep, J., Blancaflor, E. B., Hornung, E., Feussner, I., and Chapman, K. D. (2015) Lipoxygenase-derived 9-hydro(pero)xides of linoleoylethanolamide interact with ABA signaling to arrest root development during Arabidopsis seedling establishment. Plant J. 82, 315-327 CrossRef Medline

- 4. Iannotti, F. A., Di Marzo, V., and Petrosino, S. (2016) Endocannabinoids and endocannabinoid-related mediators: targets, metabolism and role in neurological disorders. Prog. Lipid Res. 62, 107-128 CrossRef Medline
- 5. Schwartz, G. J., Fu, J., Astarita, G., Li, X., Gaetani, S., Campolongo, P., Cuomo, V., and Piomelli, D. (2008) The lipid messenger OEA links dietary fat intake to satiety. Cell Metab. 8, 281-288 CrossRef Medline
- 6. McKinney, M. K., and Cravatt, B. F. (2005) Structure and function of fatty acid amide hydrolase. Annu. Rev. Biochem. 74, 411-432 CrossRef Medline
- 7. Gachet, M. S., Schubert, A., Calarco, S., Boccard, J., and Gertsch, J. (2017) Targeted metabolomics shows plasticity in the evolution of signaling lipids and uncovers old and new endocannabinoids in the plant kingdom. Sci. Rep. 7, 41177 CrossRef Medline
- 8. Chapman, K. D. (2004) Occurrence, metabolism, and prospective functions of N-acylethanolamines in plants. Prog. Lipid Res. 43, 302-327 CrossRef Medline
- 9. Blancaflor, E. B., Kilaru, A., Keereetaweep, J., Khan, B. R., Faure, L., and Chapman, K. D. (2014) N-Acylethanolamines: lipid metabolites with functions in plant growth and development. Plant J. 79, 568-583 CrossRef Medline
- 10. Wang, Y.-S., Shrestha, R., Kilaru, A., Wiant, W., Venables, B. J., Chapman, K. D., and Blancaflor, E. B. (2006) Manipulation of Arabidopsis fatty acid amide hydrolase expression modifies plant growth and sensitivity to N-acylethanolamines. Proc. Natl. Acad. Sci. U.S.A. 103, 12197-12202 CrossRef Medline
- 11. Kilaru, A., Herrfurth, C., Keereetaweep, J., Hornung, E., Venables, B. J., Feussner, I., and Chapman, K. D. (2011) Lipoxygenase-mediated oxidation of polyunsaturated N-acylethanolamines in Arabidopsis. J. Biol. Chem. 286, 15205-15214 CrossRef Medline
- 12. Bracey, M. H., Hanson, M. A., Masuda, K. R., Stevens, R. C., and Cravatt, B. F. (2002) Structural adaptations in a membrane enzyme that terminates endocannabinoid signaling. Science 298, 1793–1796 CrossRef Medline
- 13. Mileni, M., Johnson, D. S., Wang, Z., Everdeen, D. S., Liimatta, M., Pabst, B., Bhattacharya, K., Nugent, R. A., Kamtekar, S., Cravatt, B. F., Ahn, K., and Stevens, R. C. (2008) Structure-guided inhibitor design for human FAAH by interspecies active site conversion. Proc. Natl. Acad. Sci. U.S.A. 105, 12820 - 12824 CrossRef Medline
- 14. Min, X., Thibault, S. T., Porter, A. C., Gustin, D. J., Carlson, T. J., Xu, H., Lindstrom, M., Xu, G., Uyeda, C., Ma, Z., Li, Y., Kayser, F., Walker, N. P., and Wang, Z. (2011) Discovery and molecular basis of potent noncovalent inhibitors of fatty acid amide hydrolase (FAAH). Proc. Natl. Acad. Sci. U.S.A. 108, 7379 – 7384 CrossRef Medline
- 15. Blaise, M., Bailly, M., Frechin, M., Behrens, M. A., Fischer, F., Oliveira, C. L., Becker, H. D., Pedersen, J. S., Thirup, S., and Kern, D. (2010) Crystal structure of a transfer-ribonucleoprotein particle that promotes asparagine formation. EMBO J. 29, 3118-3129 CrossRef Medline
- 16. Nakamura, A., Yao, M., Chimnaronk, S., Sakai, N., and Tanaka, I. (2006) Ammonia channel couples glutaminase with transamidase reactions in GatCAB. Science 312, 1954-1958 CrossRef Medline
- 17. Fan, C., Li, Z., Yin, H., and Xiang, S. (2013) Structure and function of allophanate hydrolase. J. Biol. Chem. 288, 21422-21432 CrossRef Medline
- 18. Lee, S., Park, E.-H., Ko, H.-J., Bang, W. G., Kim, H.-Y., Kim, K. H., and Choi, I.-G. (2015) Crystal structure analysis of a bacterial aryl acylamidase belonging to the amidase signature enzyme family. Biochem. Biophys. Res. Commun. 467, 268 –274 CrossRef Medline
- 19. Holm, L., and Rosenström, P. (2010) Dali server: conservation mapping in 3D. Nucleic Acids Res. 38, W545-W549 CrossRef Medline
- 20. Kim, S.-C., Kang, L., Nagaraj, S., Blancaflor, E. B., Mysore, K. S., and Chapman, K. D. (2009) Mutations in Arabidopsis fatty acid amide hydrolase reveal that catalytic activity influences growth but not sensitivity to abscisic acid or pathogens. J. Biol. Chem. 284, 34065-34074 CrossRef Medline
- 21. Palermo, G., Bauer, I., Campomanes, P., Cavalli, A., Armirotti, A., Girotto, S., Rothlisberger, U., and De Vivo, M. (2015) Keys to lipid selection in fatty acid amide hydrolase catalysis: structural flexibility, gating residues and multiple binding pockets. PLoS Comput. Biol. 11, e1004231 CrossRef Medline



- 22. Teplitski, M., Mathesius, U., and Rumbaugh, K. P. (2011) Perception and degradation of N-acyl homoserine lactone quorum sensing signals by mammalian and plant cells. Chem. Rev. 111, 100-116 CrossRef Medline
- 23. Palmer, A. G., Senechal, A. C., Mukherjee, A., Ané, J.-M., and Blackwell, H. E. (2014) Plant responses to bacterial N-acyl L-homoserine lactones are dependent on enzymatic degradation to L-homoserine. ACS Chem. Biol. 9, 1834-1845 CrossRef Medline
- 24. Shrestha, R., Dixon, R. A., and Chapman, K. D. (2003) Molecular identification of a functional homologue of the mammalian fatty acid amide hydrolase in Arabidopsis thaliana. J. Biol. Chem. 278, 34990-34997 CrossRef Medline
- 25. Cudney, R., Patel, S., Weisgraber, K., Newhouse, Y., and McPherson, A. (1994) Screening and optimization strategies for macromolecular crystal growth. Acta Crystallogr. D Biol. Crystallogr. 50, 414-423 CrossRef
- 26. Otwinowski, Z., and Minor, W. (1997) Processing of X-ray diffraction data collected in oscillation mode. Methods Enzymol. 276, 307-326 CrossRef
- 27. Matthews, B. W. (1968) Solvent content of protein crystals. J. Mol. Biol. 33, 491-497 CrossRef Medline
- 28. McCoy, A. J., Grosse-Kunstleve, R. W., Adams, P. D., Winn, M. D., Storoni, L. C., and Read, R. J. (2007) Phaser crystallographic software. J. Appl. Crystallogr. 40, 658 – 674 CrossRef Medline
- 29. Emsley, P., and Cowtan, K. (2004) Coot: model-building tools for molecular graphics. Acta Crystallogr. D Biol. Crystallogr. 60, 2126-2132 CrossRef Medline
- 30. Murshudov, G. N., Vagin, A. A., and Dodson, E. J. (1997) Refinement of macromolecular structures by the maximum-likelihood method. Acta Crystallogr. D Biol. Crystallogr. 53, 240 - 255 CrossRef Medline
- 31. Adams, P. D., Afonine, P. V., Bunkóczi, G., Chen, V. B., Davis, I. W., Echols, N., Headd, J. J., Hung, L.-W., Kapral, G. J., Grosse-Kunstleve, R. W., Mc-Coy, A. J., Moriarty, N. W., Oeffner, R., Read, R. J., Richardson, D. C., et al. (2010) PHENIX: a comprehensive Python-based system for macromolecular structure solution. Acta Crystallogr. D Biol. Crystallogr. 66, 213-221 CrossRef Medline

- 32. Laskowski, R. A., MacArthur, M. W., Moss, D. S., and Thornton, J. M. (1993) PROCHECK: a program to check the stereochemical quality of protein structures. J. Appl. Crystallogr. 26, 283-291 CrossRef
- 33. Moriarty, N. W., Draizen, E. J., and Adams, P. D. (2017) An editor for the generation and customization of geometry restraints. Acta Crystallogr. D Struct. Biol. 73, 123-130 CrossRef Medline
- 34. Moriarty, N. W., Grosse-Kunstleve, R. W., and Adams, P. D. (2009) electronic Ligand Builder and Optimization Workbench (eLBOW): a tool for ligand coordinate and restraint generation. Acta Crystallogr. D Biol. Crystallogr. 65, 1074-1080 CrossRef Medline
- 35. Patricelli, M. P., Lashuel, H. A., Giang, D. K., Kelly, J. W., and Cravatt, B. F. (1998) Comparative characterization of a wild type and transmembrane domain-deleted fatty acid amide hydrolase: identification of the transmembrane domain as a site for oligomerization. Biochemistry 37, 15177-15187 CrossRef Medline
- 36. Kim, S.-C., Faure, L., and Chapman, K. D. (2013) Analysis of fatty acid amide hydrolase activity in plants. Methods Mol. Biol. 1009, 115-127 CrossRef Medline
- Schrödinger, LLC (2018) Maestro, Release 2018-1, Schrödinger, LLC, New York
- 38. Chemical Computing Group ULC (2018) Molecular Operating Environment (MOE), Version 2013.08, Chemical Computing Group ULC, Montreal, Quebec, Canada
- Jones, G., Willett, P., Glen, R. C., Leach, A. R., and Taylor, R. (1997) Development and validation of a genetic algorithm for flexible docking. J. Mol. Biol. 267, 727-748 CrossRef Medline
- 40. Liebeschuetz, J. W., Cole, J. C., and Korb, O. (2012) Pose prediction and virtual screening performance of GOLD scoring functions in a standardized test. J. Comput. Aided Mol. Des. 26, 737-748 CrossRef Medline
- 41. Bowers, K. J., Chow, E., Xu, H., Dror, R. O., Eastwood, M. P., Gregersen, B. A., Klepeis, J. L., Kolossvary, I., Moraes, M. A., and Sacerdoti, F. D. (2006) Scalable algorithms for molecular dynamics simulations on commodity clusters, in Proceedings of the 2006 ACM/IEEE Conference on Supercomputing, Tampa, November 11–17, 2006, Article 84, Association for Computing Machinery (ACM), New York



Structural analysis of a plant fatty acid amide hydrolase provides insights into the evolutionary diversity of bioactive acylethanolamides

Mina Aziz, Xiaoqiang Wang, Ashutosh Tripathi, Vytas A. Bankaitis and Kent D. Chapman

J. Biol. Chem. 2019, 294:7419-7432. doi: 10.1074/jbc.RA118.006672 originally published online March 20, 2019

Access the most updated version of this article at doi: 10.1074/jbc.RA118.006672

Alerts:

- · When this article is cited
- · When a correction for this article is posted

Click here to choose from all of JBC's e-mail alerts

This article cites 38 references, 10 of which can be accessed free at http://www.jbc.org/content/294/18/7419.full.html#ref-list-1